arXiv:2101.01821v1 [cond-mat.mtrl-sci] 5 Jan 2021

The molecular origin of Frenkel biexciton binding

Elizabeth Gutiérrez Meza,[1], Ravyn Malatesta,[1] Hongmo Li,[2]
Ilaria Bargigia,[3] Ajay Ram Srimath Kandada,[3],
David A. Valverde-Chávez,[1] Natalie Stingelin,[2,4]
Sergei Tretiak,[5,6,7] Eric R. Bittner,[8†] and Carlos Silva[1,2,9*]

[1]School of Chemistry and Biochemistry, Georgia Institute of Technology,
901 Atlantic Drive, Atlanta, GA 30332, United States
[2]School of Materials Science and Engineering, Georgia Institute of Technology,
North Avenue, Atlanta, GA 30332, United States
[3]Department of Physics and Center for Functional Materials, Wake Forest University,
1834 Wake Forest Road, Winston-Salem, NC 27109, United States
[4] School of Chemical and Biomolecular Engineering,
311 Ferst Drive NW, Atlanta, GA 30332, United States
[5]Theoretical Division, Los Alamos National Laboratory,
Los Alamos, NM 87545, United States
[6]Center for Nonlinear Studies, Los Alamos National Laboratory,
Los Alamos, NM 87545, United States
[7]Center for Integrated Nanotechnologies, Los Alamos National Laboratory,
Los Alamos, NM 87545, United States
[8]Department of Chemistry, University of Houston, Houston, Texas 77204, United States
[9]School of Physics, Georgia Institute of Technology, 837 State Street,
Atlanta, GA 30332, United States

[†]E-mail address: ebittner@central.uh.edu
[*]Corresponding author; E-mail address: carlos.silva@gatech.edu

Frenkel excitons are primary photoexcitations in molecular semiconductors and are unequivocally responsible for their optical properties. However, the spectrum of corresponding biexcitons — bound exciton pairs — has not been resolved thus far in organic materials. We correlate the energy of two-quantum exciton resonances with that of the single-quantum transition by means of nonlinear coherent spectroscopy. Using a Frenkel exciton model, we relate the biexciton binding energy to the magnitude and the sign of the exciton-exciton interaction energy and the inter-site hopping energy, which are molecular parameters that can be quantified by quantum chemistry. Unexpectedly, excitons with *interchain* vibronic dispersion reveal *intrachain* biexciton correlations, and vice-versa. The details of biexciton correlations determine exciton bimolecular annihilation, which is ubiquitous in organic semiconductors. It is crucial to quantify these interactions in order to establish a quantum-mechanical basis for their rate constants. Our work enables new opportunities for general insights into the many-body electronic structure in molecular excitonic systems such as organic semiconductor crystals, molecular aggregates, photosynthetic light-harvesting complexes, and DNA.

Many-body electronic correlations are ubiquitous in semiconductors and dominate the optical properties of organic solids (*1*). For example, the spontaneous formation of strongly-coupled light-matter quantum condensates in organic materials depends fundamentally on the details of exciton-exciton interactions (*2*). The primary photoexcitations in organics semiconductors are localized molecular electronic singlet excitations (S_1) termed Frenkel excitons (*3*), and here we report the first direct spectroscopic observation of Frenkel biexcitons — bound two-exciton quasiparticles ($[2\,S_1]^{\ddagger}$) — in a macromolecular solid. While ample theoretical work points towards their existence in organic solids (*4–11*), and in optical lattices (*12*), thus far the only

report of the observation of such species is in solid argon (*13*). Quantifying the factors that govern biexciton stability is fundamentally important because they reveal intricate details of the dipolar nature of excitons, which are deterministic in the optical properties of organic semiconductors. There is ample indirect evidence of the dynamic formation of exciton two-quantum states by incoherent, sequential ultrafast excitation in semiconductor polymers (*14–16*). Aside from their fundamental importance in that biexcitons provide a sophisticated probe of electronic structure, they are consequential intermediates in a wide range of photophysical processes such as exciton dissociation into electrons (e^-) and holes (h^+) [$S_0 + 2\,\hbar\omega \longrightarrow [2\,S_1]^\ddagger \longrightarrow 2\,e^- + 2\,h^+$] (*14*), bimolecular annihilation [$S_1 + S_1 \longrightarrow [2\,S_1]^\ddagger \longrightarrow S_0 + S_0$] (*15*), and singlet fission producing triplet (T_1) states [$S_0 + 2\,\hbar\omega \longrightarrow [2\,S_1]^\ddagger \longrightarrow 2\,T_1 + 2\,T_1$] (*16*).

Here we report the coherent, nonlinear optical spectrum of Frenkel biexcitons in a model semiconductor polymer (*17*), [poly(2,5-bis(3-hexadecylthiophene-2-yl)thieno[3,2-b]thiophene)] — PBTTT. We selected this material due to its thermotropic phase behavior, hosting liquid-crystalline phases at temperatures above ambient conditions (*18,19*), which renders the polymer system highly dynamic. We observe spectral structure that is buried within the linear excitation lineshape, which reflects both attractive and repulsive biexciton correlations. We develop a Frenkel exciton model that quantifies how the balance of exciton-exciton correlation energy, the energetic fluctuations between different sites in the polymer aggregate, and exciton delocalization establish biexciton stability. Our measurements reveal microscopic criteria for both attractive and repulsive Frenkel-biexciton binding in macromolecular semiconductors.

In photophysical aggregates of semiconductor polymers, Frenkel excitons consist of chromophoric photoexcitations localized over at most a few sub-units both along the polymer chain (categorized as a J-aggregate state) or between multiple polymer chains (H aggregate) (*20*), with hybrid HJ structure (*21*). Since the transition moment is typically oriented parallel to the polymer chains, excitons delocalized along the chain form J-aggregate states and have negative

intersite hopping integral t, while excitons delocalized across multiple chains form H-aggregate states and have a positive t. Such states are depicted in Fig. 1, which shows the potential scenarios for *biexciton* interactions between pairs of H-like and J-like excitons. The small ellipsoids represent the molecular sub-units, while the larger ellipsoids represent single electron/hole excitons delocalized over multiple sites either between chains (Fig. 1A, B) or along the chains (Fig. 1C, D). The latter of these form a quantum mechanical basis for biexciton formation.

Exciton pairs become bound when their mutual attraction overcomes both the energy barrier imposed by local energetics and their relative kinetic energy. However, there is a subtlety concerning the hopping integral t, which related to the free-exciton bandwidth $W = 4|t|$ and hence the exciton effective mass $\mu_{\text{eff}} = -\hbar^2/2t$, and the interaction energy U. These parameters *must* have the *same* signs to produce a bound species. We note that *both* attractive and repulsive interactions can produce bound states. To see this, consider the solutions of the one-dimensional Schrödinger equation with a δ-function potential:

$$t\psi''(x) + U\delta(x)\psi(x) = E\psi(x). \tag{1}$$

This system has a single bound state $\psi(x)$ which vanishes as $x \to \pm\infty$ and has an exponential form $\psi(x) = \sqrt{\kappa}e^{-\kappa|x|}$, where $\kappa = U/2t$ is a positive constant and $E = t\kappa^2$. Ordinarily, we set $t < 0$ and $U < 0$ producing a single state energetically below the $E > 0$ scattering states. However, bound states can also occur when $t > 0$ and $U > 0$. Such states would occur at the above top of the energy band for free biexcitons.

Curiously, H-aggregate excitons can move parallel to the chains with transfer integral $t < 0$. Moreover, the orientation of the local exciton dipoles give $U < 0$, implying that H-like exciton pairs can form bound biexcitons with an *attractive* binding energy *below* that of the energy for free H-like exciton pairs. On the contrary, J-like excitons can move perpendicular to the chains with transfer integral $t > 0$ and with contact interaction $U > 0$. This implies that the bound

J-like biexciton states can form *above* the continuum for free J-like exciton pairs. Because of the *hybrid* HJ aggregate nature (*21*) established in PBTTT (*22*), both H-like and J-like behavior can be observed offering the possibility of observing both 2J and 2H biexcitons within the same system.

To pursue this in a many-body theoretical frame work, we developed two-band Hubbard-like model with Hamiltonian

$$\hat{H} = E_0 + \Delta \sum_{j=1}^{N} (-1)^j \hat{c}_j^\dagger \hat{c}_j + t \sum_{j=1}^{N} (\hat{c}_j^\dagger \hat{c}_{j+1} + \hat{c}_{j+1}^\dagger \hat{c}_j) + U \sum_{j=1}^{N} \hat{c}_j^\dagger \hat{c}_j \hat{c}_{j+1}^\dagger \hat{c}_{j+1}. \tag{2}$$

The operators $\{\hat{c}_i, \hat{c}_j^\dagger\} = \delta_{ij}$ describe the creation of an exciton in site i and removal from site j, and in which odd-numbered sites correspond to sub-unit A and even-numbered sites correspond to sub-unit B. Periodic boundary conditions are such that $\hat{c}_N = \hat{c}_1$ and Pauli exclusion prevents any single site from being occupied by more than a single exciton. Our model accounts for energetic differences between repeating units, $\pm\Delta$, which we refer to as the *crenelation*. The parameters t and U, which we will take to be short ranged and due to contact interaction between excitons on neighboring sites, are as defined in eq. 1. This model is consistent with the more elaborate one of Gallagher and Spano (*8*), but it captures the salient physics relevant to Frenkel biexciton stability and readily incorporates effects of crenelation, relevant to the incorporation fluctuations in site energy.

For dissociated pairs, we can ignore the contact interaction and set $U = 0$ to obtain $E_{\text{free}}/t = 2\sqrt{(\Delta/t)^2 + 4}$ as the limiting case for two excitons with bulk momentum $k = 0$. On the other hand, the contact potential produces a single bound biexciton state with binding energy of $E_b/t = (U/2t)^2$. Exciton pairs are bound once $E_b < E_{\text{free}}$ (for the 2J). This gives that the critical value of the coupling varies as Δ^2. Hence, crenelation destabilizes the exciton binding suggesting that a highly crenelated lattice would disfavour biexciton binding. Fig. 2(E) shows the two asymptotic limits of our model given as dashed curves and results from a numerically

exact diagonalization of the a two-band Hubbard-like Hamiltonian. For our numerical studies we set both $U < 0$ and $t < 0$ so that the bound 2H-biexciton would be found at the bottom of the energy spectrum. The 2J case is identical except for a sign-change in the energy axis producing a bound 2J state at the top of the energy spectrum. (See Supplemental Material for additional details.)

Semiconductor polymers exhibit a disordered energy landscape, which is reflected as a random variation in the site energies in our model. To examine this, we write $\Delta_n = \bar{\Delta} + \delta\Delta_n$ where $\overline{\delta\Delta_n \delta\Delta_{n'}} = \sigma_\Delta^2 \delta_{nn'}$ gives the variance for a normal distribution with $\overline{\delta\Delta_n} = 0$. Fig. 1F shows the probability of biexciton formation for various values of the interaction strength U and for increasing levels of site-wise energy fluctuations. The results indicate that bound biexcitons are robust against local energy disorder. Generally, disorder destabilizes the bound biexciton state. However, we also note that for extremely weakly interacting excitons, local disorder can *enhance* the formation of bound pairs when U is close to the stability threshold. This can occur if neighboring sites have a fortuitously small enough energy off-set to form a local trapping site for a bound biexciton. However, the lineshape for these biexcitons will be broad to reflect the inhomogeneous distribution of their energies.

Fig. 2A shows the chemical structure of a PBTTT oligomer with three repeating units as optimized using DFT (B3LYP/6-31G*). Superimposed are the ground and excited state static dipoles which are largely oriented perpendicular to the long molecular axis. These are highly sensitive to the instantaneous configurations adopted by the chain and average to zero over all chain conformations in the bulk system. Shown also is the $S_0 \rightarrow S_1$ transition dipole moment which is oriented along the long molecular axis.

From the linear spectrum in Fig. 2B, we observe a dominant H-aggregate character as the peak at ~ 2.06 eV which corresponds to the 0–0 vibronic peak, is suppressed with respect to the rest of the vibronic progression (*21*). This corresponds to the situation in Fig. 1A for a *single*

exciton. We can estimate $W = 4|t| \approx 60$ meV, expressed via the 0–0/0–1 absorbance ratio (*23*), and thus that $t \approx 15$ meV. We have previously demonstrated that predominantly J-aggregate character can be induced by blending the same material with polyethyleneoxide (*22*). The 0–0 absorbance peak red-shifts by $\sim$ 70–80 meV in that case.

To quantify biexciton spectral structure, we implement coherent two-dimensional photoluminescence excitation (2D-PLE) spectroscopy on PBTTT. Such measurements can directly identify biexciton resonances via two-quantum coherences (details in Supplementary Material), and can thus quantify their binding energies (*24–26*). In this work, the coherent two-dimensional excitation spectrum is constructed via incoherent measurement of the time-integrated photoluminescence (PL) intensity due to a fourth-order excited-state population arising from the interference of wavepackets produced by a sequence of four light-matter interactions (*27*). With this technique, we measure spectral correlations between coherences involving pulses 1 and 2 and those corresponding to pulses 3 and 4 in Fig. 3A. The two energy axes are constructed by Fourier transformation of the two-dimensional coherence decay function along time variables t_{21} and t_{43} at a fixed population time t_{32}. The spectral correlation along resulting energy axes ($\hbar\omega_{21}$, $\hbar\omega_{43}$) involve single-quantum ($|0\rangle \rightarrow |1\rangle$) and two-quantum ($|0\rangle \rightrightarrows |2\rangle$) transitions, represented schematically in the left of Fig. 3B. The two principal coherent pathways involving the correlations between one- and two-quantum coherences under this detection scheme are depicted by the double-sided Feynman diagrams in Fig. 3B. In Figs. 3C and 3D we represent, respectively, a schematic diagram of the one- and two-quantum 2D-PLE coherent spectra for two transitions correlated via a common ground state such as H-like and J-like states in a HJ aggregate, each evident in the diagonal of the 2D-PLE spectrum ($\hbar\omega_{21} = \hbar\omega_{43}$). In addition, the spectral correlation between these two peaks is manifested by cross peaks between the diagonal features. In the two-quantum correlation spectrum, signal along the two-quantum diagonal ($\hbar\omega_{21-2Q} = 2\hbar\omega_{43}$) signify two non-interacting excitons, while signal above or below the di-

agonal signifies binding interactions with repulsive or attractive character, depending on the signs of t and U (H- or J-like coupling), respectively. In our schematic in Fig. 3D, the lower energy diagonal peak displays 2H biexcitons (the two-quantum energy is higher than twice the one-quantum energy), while the higher-energy resonance displays structure corresponding to 2J biexcitons (in which the two-quantum energy is less than twice the one-quantum energy.

We first focus on the single-quantum 2D-PLE lineshape in Fig. 4A. We note that the spectral range in of the measurement, limited by the femtosecond laser spectrum displayed in Fig. 2B, overlaps with the full origin (0–0) absorption line. The 2D spectrum is dominated by a symmetric diagonal peak centered at $\hbar\omega_{21} = \hbar\omega_{43} \approx 2.06\,\text{eV}$, corresponding to the 0–0 peak energy. We also observe a weak diagonal signal centered at $\sim 1.99\,\text{eV}$, with even weaker structure identified at lower energy. These features display intense cross peaks with the (0–0) resonance. The rich spectral structure displayed at the low energy tail of the 2D-PLE spectrum is not evident in the featureless linear absorption spectrum, and demonstrates the existence of distinct states at the low-energy edge of the 0–0 absorption peak. We note that energy of the weak diagonal feature corresponds to the 0–0 absorbance peak energy in PBTTT J aggregates induced in polar polymer blends (*22*). We thus hypothesize that these are weak signatures of J-aggregate macromolecular conformations.

We next examine two-quantum correlations within the spectral structure in Fig. 4B, looking for exciton-exciton resonances that display repulsive or attractive biexciton binding energies as depicted in Fig. 3D. Most prominently, we observe a broad distribution along the two-quantum energy axis $\hbar\omega_{21,2Q}$ centered at the one-quantum energy $\hbar\omega_{43} = 2.06\,\text{eV}$ (the 0–0 excitation maximum), with the peak of the distribution below the two-quantum diagonal, *i.e.*, below the energy at which $\hbar\omega_{21,2Q} = 2\hbar\omega_{43}$. Nevertheless, the spectrum cuts through the diagonal line, with a tail extending to the high-energy side of the diagonal. We also observe two-quantum peaks for the features at lower energy than the 0–0 peak in Fig. 4A. These are both centered

at higher energy than the diagonal; the two-quantum correlation is predominantly repulsive for the low-energy features.

In Fig. 4D we display cuts of the two-quantum excitation spectrum at a fixed one-quantum energies $\hbar\omega_{43}$. The cuts are along $\hbar\omega_{21,2Q}$ relative to the two-quantum diagonal energy $\hbar\omega_{\mathrm{diag}}$. This is a good reference because signal on the diagonal corresponds to the energy of two excitons that coexist without interaction. We discuss the structure in Fig. 4D in detail in the Supplemental Material, but we notice that the 0–0 absorption peak, assigned to the vibronic progression of an H aggregate (*21*), forms biexcitons with *attractive* interactions with $E_{2\mathrm{J,b}} = -64 \pm 6$ meV. On the other hand, the low-energy resonances, which we have hypothesized to correspond to J-aggregate resonances, display predominantly *repulsive* two-quantum correlations, peaked at $E_{2\mathrm{H,b}} = +106 \pm 6$ and $+233 \pm 6$ meV, respectively. Fig. 4 thus demonstrates that both attractive and repulsive biexciton binding coexist within the inhomogeneously broadened 0–0 linear absorption peak. Given $E_{2\mathrm{J,b}}$, corresponding to the correlated biexciton at the origin of the H-aggregate progression, and the estimate of t_H from its linear lineshape in Fig. 2B, we determine that $U/t_H = 4.15$, placing the biexciton well into the range of stable biexcitons (see phase diagram in Supplemental Material). For the biexciton associated with the J aggregate, we do not have a direct measurement of t_J, but we can speculate that it is a fraction of t_H given the predominance of H-like character (*20*), placing J-like biexcitons also well within the stable (but repulsive) binding region, as depicted in Fig. 1.

The complex spectral structure due to hybrid HJ excitons (*21*), that are not resolved within the inhomogeneously-broadened linear absorption lineshape, are revealed using nonlinear coherent spectroscopy. All excitons also reveal corresponding biexcitons; however, it is surprising that H-like excitons appear to do so via *intrachain* exciton-exciton couplings. In contrast, J-like excitons appear to do so through *interchain* coupling. In either case, the biexciton binding energy is related to the exciton-exciton contact interaction U and the inter-site hopping energy

t, which are molecular parameters quantified by quantum chemistry. The insights presented in this report open opportunities to design and predict the stability of Frenkel biexcitons in polymeric semiconductors, and more generally, to explore in unprecedented depth the many-body electronic structure of any material in which Frenkel excitons are the primary photoexcitations, including a broader class of organic semiconductors (*1*), molecular aggregates (*28*), photosynthetic light-harvesting complexes (*29*), and DNA (*30*).

References

1. V. M. Agranovich, *Excitations in organic solids*, vol. 142 (OUP Oxford, 2009).

2. J. Keeling, S. Kéna-Cohen, *Annu. Rev. Phys. Chem.* **71**, 435 (2020).

3. V. Agranovich, B. Toshich, *Sov. Phys. JETP* **26**, 104 (1968).

4. D. Fox, *Mol. Cryst. Liq. Cryst.* **57**, 39 (1980).

5. F. C. Spano, V. Agranovich, S. Mukamel, *J. Chem. Phys.* **95**, 1400 (1991).

6. G. Vektaris, *J. Chem. Phys.* **101**, 3031 (1994).

7. F. Guo, M. Chandross, S. Mazumdar, *Phys. Rev. Lett.* **74**, 2086 (1995).

8. F. B. Gallagher, F. C. Spano, *Phys. Rev. B* **53**, 3790 (1996).

9. S. Mazumdar, F. Guo, K. Meissner, B. Fluegel, N. Peyghambarian, *J. Chem. Phys.* **104**, 9292 (1996).

10. V. Agranovich, O. Dubovsky, D. Basko, G. La Rocca, F. Bassani, *J. Lumin.* **85**, 221 (2000).

11. G. Kun, *et al.*, *Chin. Phys. B* **18**, 2961 (2009).

12. P. Xiang, M. Litinskaya, R. V. Krems, *Phys. Rev. A* **85**, 061401 (2012).

13. Y. Baba, G. Dujardin, P. Feulner, D. Menzel, *Phys. Rev. Lett.* **66**, 3269 (1991).

14. C. Silva, *et al.*, *Phys. Rev. B* **64**, 125211 (2001).

15. M. A. Stevens, C. Silva, D. M. Russell, R. H. Friend, *Phys. Rev. B* **63**, 165213 (2001).

16. C. Silva, *et al.*, *J. Phys.: Condens. Matter* **14**, 9803 (2002).

17. I. McCulloch, *et al.*, *Nat. Mater.* **5**, 328 (2006).

18. M. L. Chabinyc, M. F. Toney, R. J. Kline, I. McCulloch, M. Heeney, *J. Am. Chem. Soc.* **129**, 3226 (2007).

19. D. M. Delongchamp, *et al.*, *Macromolecules* **41**, 5709 (2008).

20. F. Paquin, *et al.*, *Phys. Rev. B* **88**, 155202 (2013).

21. F. C. Spano, C. Silva, *Annu. Rev. Phys. Chem.* **65**, 477 (2014).

22. C. Hellmann, *et al.*, *Adv. Mater.* **25**, 4906 (2013).

23. J. Clark, C. Silva, R. H. Friend, F. C. Spano, *Phys. Rev. Lett.* **98**, 206406 (2007).

24. K. W. Stone, D. B. Turner, K. Gundogdu, S. T. Cundiff, K. A. Nelson, *Acc. Chem. Res.* **42**, 1452 (2009).

25. D. B. Turner, K. A. Nelson, *Nature* **466**, 1089 (2010).

26. F. Thouin, *et al.*, *Phys. Rev. Materials* **2**, 034001 (2018).

27. P. F. Tekavec, G. A. Lott, A. H. Marcus, *J. Chem. Phys.* **127**, 214307 (2007).

28. N. J. Hestand, F. C. Spano, *Acc. Chem. Res.* **50**, 341 (2017).

29. G. D. Scholes, G. R. Fleming, A. Olaya-Castro, R. Van Grondelle, *Nat. Chem.* **3**, 763 (2011).

30. E. R. Bittner, *J. Chem. Phys.* **125**, 094909 (2006).

Acknowledgments

The authors are grateful to Prof. Martin Heeney for providing the material used for this work. **Funding:** The work at Georgia Tech was funded by the National Science Foundation (DMR-1904293 [Silva] and DMREF-1729737 [Stingelin, Silva]). C.S. acknowledges support from the the School of Chemistry and Biochemistry and the College of Science at Georgia Tech. The work at the University of Houston was funded in part by the National Science Foundation (CHE-1664971, DMR-1903785) and the Robert A. Welch Foundation (E-1337). **Author contributions:** I.B. and A.R.S.K. constructed the 2D-PLE setup. The development of the demodulation technique to measure two-quantum coherent spectra was carried out by E.G.M., R.M., and D.A.V.C., aided by I.B. and supervised by C.S. and A.R.S.K. H.L. processed the samples, supervised by N.S. E.G.M measured and analyzed the 2D coherent excitation spectra, aided by D.A.V.C. and supervised by C.S. H.L. carried out the DFT calculations, supervised by S.T. E.R.B. developed the theoretical concepts and carried out the analysis. The intellectual basis for this paper was conceived by C.S., A.R.S.K., and E.R.B. All co-authors participated in the redaction of the manuscript. **Competing interests:** The authors declare no competing interests. **Data and materials availability:** Raw data is available from the corresponding author by appropriate request.

Supplementary Materials

Materials and Methods

2D-PLE Supplementary Results

Supplementary Theoretical Modelling

Figures S1–S7

Table S1

References 31–37

Figures

Figure 1: Theoretical model for biexciton formation. (A-D) H- vs J- biexciton configurations. In A & B, H-like excitons are delocalized along the π-stacking direction the polymer chains and move along the chain with hopping integral $t < 0$. Here, exciton dipoles are aligned to produce an attractive $U < 0$ contact interaction. In comparison, the J-like excitons depicted in C & D move between chains with $t > 0$ and exciton dipole are aligned co-facially to produce a repulsive $U > 0$ contact interaction. (E) Free vs. bound biexciton energies. The energy of a free pair excitons is determine by their band-width whereas the binding energy is determined by the contact interaction U. Bound biexcitons become stable once $E_B < E_{\text{free}}$. Points correspond to energies from numerical diagonalization while dashed curves are the asymptotic limits. The gray-dashed line is for two free excitons on a homogeneous lattice ($\Delta = 0$). (F) Probability for biexciton formation for energetically disordered lattices. Here we set $\Delta/t = 1$ and increase the variance in the local site energy. Curves are labeled by the interaction U for $U/t = 2.5$ to $U/t = 2.1$.

Figure 2: Photophysical structure of PBTTT. (A) Calculated orientation of the transition dipole moment (T), as well as the ground- and excited-state dipoles (GS, ES) for a trimer, for the particular configuration shown here. The angle of the ground-state dipole with respect to the transition dipole is 79.3° and that for the excited-state dipole is 99.5°. The amplitudes of the ground state, excited state, and transition dipole moment are 0.98 D, 0.93 D, and 18.29 D, respectively. The dipoles are not drawn to scale. (B) Linear absorption spectrum of PBTTT measured at 5 K. Superimposed is the spectrum of the femtosecond pulse train used for the measurements presented in Fig. 4.

Figure 3: Two-dimensional coherent photoluminescence excitation (2D-PLE) spectroscopy. (A) Schematic of the experimental pulse sequence. Here ϕ_i is the phase of pulse $i = 1, 2, 3, 4$. The inter-pulse delays are t_{21} (coherence time), t_{32} (population waiting time), and t_{43} (coherence time). The phase-modulation reference waveforms for phase-sensitive detection are generated optically at frequencies Ω_{21} and Ω_{43}, at which the relative phase $\phi_{21} = \phi_2 - \phi_1$ and $\phi_{43} = \phi_4 - \phi_3$ oscillate, respectively. In this work, time- and spectrally integrated photoluminescence (PL) intensity is demodulated by phase-sensitive detection at the reference frequency $f_{\rm ref} = \Omega_{43} + \Omega_{21}$ and $\Omega_{43} + 2\Omega_{21}$ for the one- and two-quantum correlation spectra, respectively, shown in Fig. 4. (B) Double-sided Feynman diagrams of the two most important two-quantum response terms that couple a ground state ($|0\rangle$), a single exciton state ($|1\rangle$), and a two-exciton state ($|2\rangle$). (C) Schematic representation of the 2D-PLE expected spectrum for two correlated optical transitions at energies $\hbar\omega_a$ and $\hbar\omega_b$. The spectral axes $\hbar\omega_{21}$ and $\hbar\omega_{43}$ are obtained by Fourier transform of the 2D coherent PL decay function along time variables t_{21} and t_{43} at fixed t_{32}. (D) Schematic representation of a two-quantum 2D-PLE correlatios spectrum. The two-quantum energy $\hbar\omega_{21,2Q}$ corresponds to the two quantum coherences involving pulses 1 and 2, The diagonal line represents $\hbar\omega_{21,2Q} = 2\hbar\omega_{43}$.

Figure 4: 2D-PLE spectra measured at 5 K and $t_{32} = 30$ fs. (A) The real part of the one-quantum non-rephasing ($f_{\rm ref} = \Omega_{43} + \Omega_{21}$) spectrum. (B) The real part of the two-quantum ($f_{\rm ref} = \Omega_{43} + 2\Omega_{21}$)) spectrum. (C) Diagrammatic representation involving the optical transitions associated with the interpretation of the spectrum in B. (D) Spectral cuts along $\hbar\omega_{21,2Q} - \hbar\omega_{\rm diag}$ spectral axis at fixed $\hbar\omega_{43} = 2.06$ (blue), 1.99 (fuscia), and 1.94 eV (red) for the spectrum in B. Here $\hbar\omega_{\rm diag}$ is the $\hbar\omega_{21,2Q} = 2\hbar\omega_{43}$ two-quantum diagonal energy, corresponding to zero net two-quantum correlation energy (neither binding nor repulsion).

Figure 1

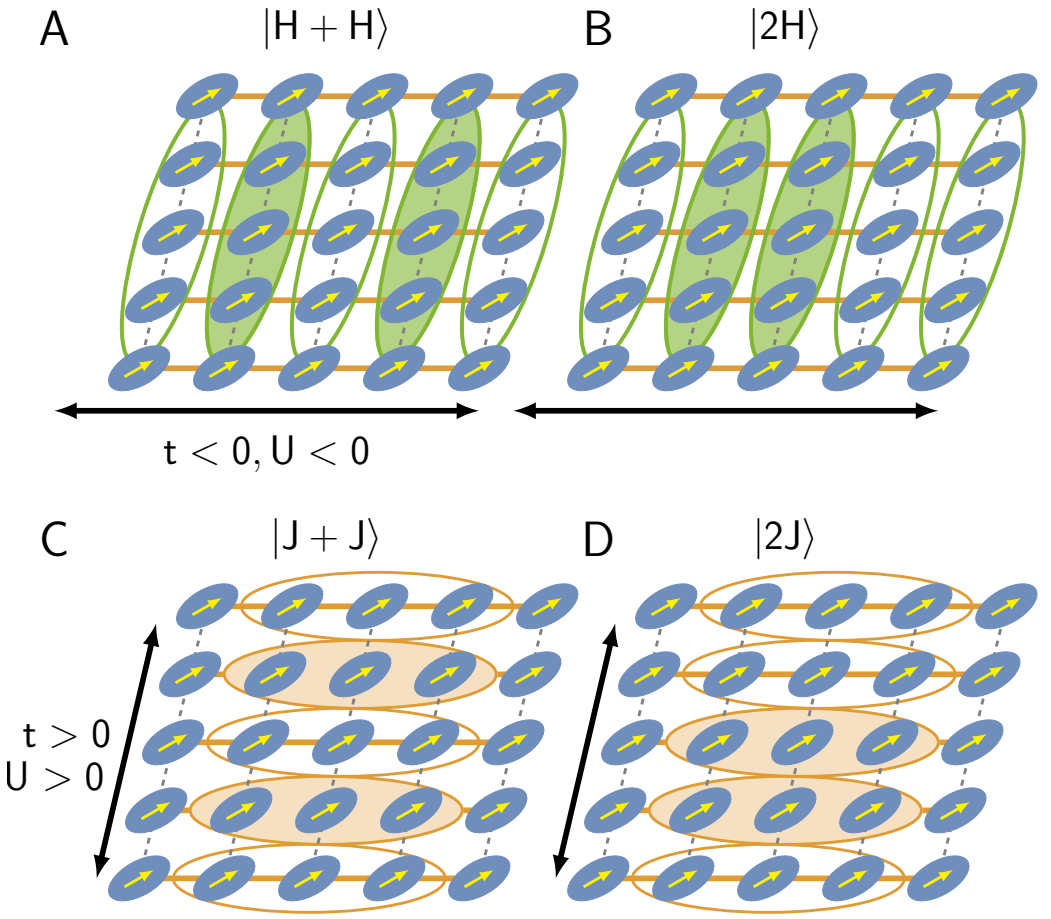
A
|H + H⟩
B
|2H⟩
t < 0, U < 0
C
|J + J⟩
D
|2J⟩
t > 0
U > 0

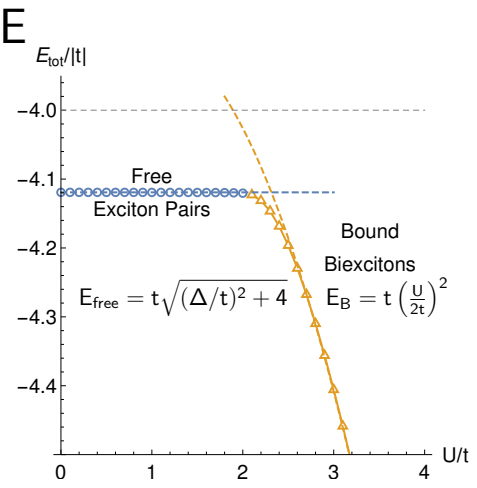
E
E_tot/|t|
−4.0
−4.1
−4.2
−4.3
−4.4
Free
Exciton Pairs
Bound
Biexcitons
E_free = t√((Δ/t)² + 4)
E_B = t (U/2t)²
0
1
2
3
4
U/t

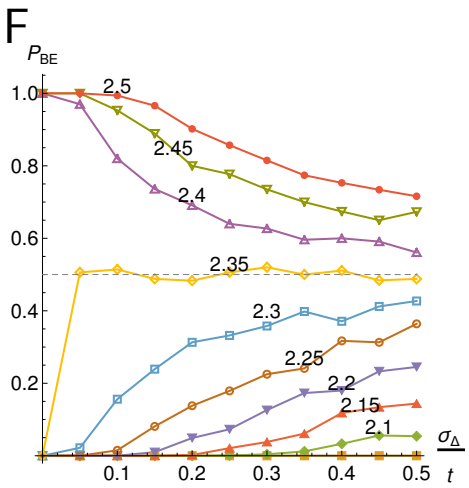
F
P_BE
1.0
0.8
0.6
0.4
0.2
2.5
2.45
2.4
2.35
2.3
2.25
2.2
2.15
2.1
0.1
0.2
0.3
0.4
0.5
σ_Δ / t

Figure 2

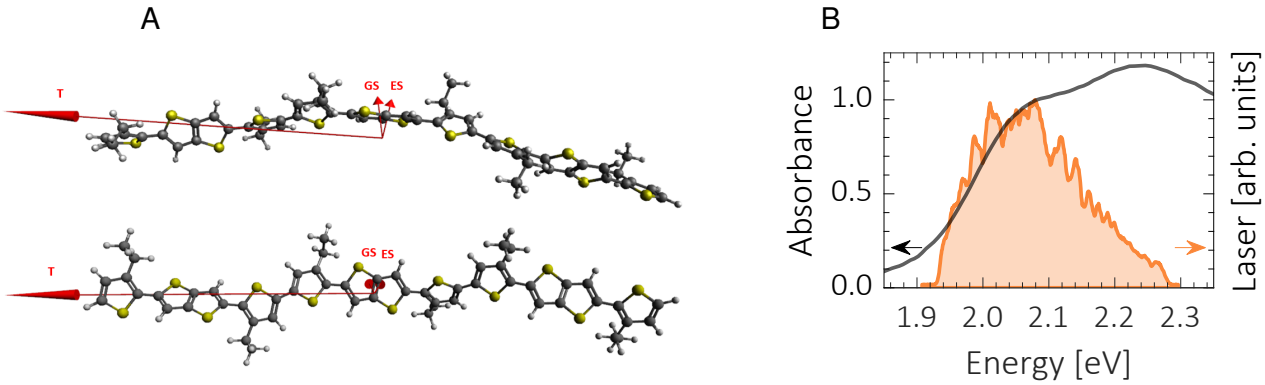
A
T
GS
ES
T
GS
ES
B
Absorbance
1.0
0.5
0.0
1.9
2.0
2.1
2.2
2.3
Energy [eV]
Laser [arb. units]

Figure 3

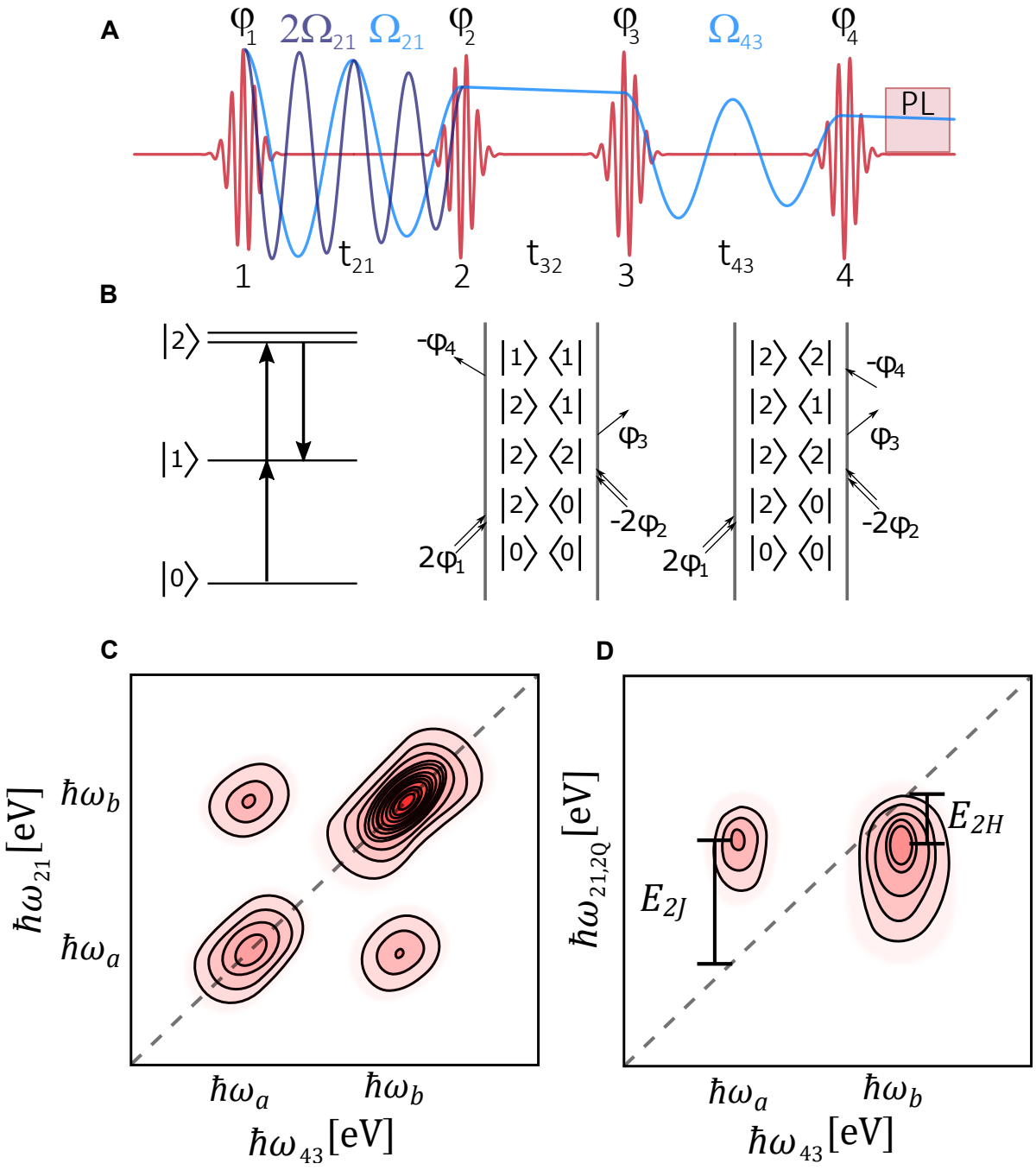
A
φ1
2Ω21
Ω21
φ2
φ3
Ω43
φ4
PL
t21
t32
t43
1
2
3
4
B
|2⟩
|1⟩
|0⟩
-φ4
φ3
-2φ2
2φ1
C
ħω_b
ħω_21 [eV]
ħω_a
ħω_a
ħω_b
ħω_43 [eV]
D
ħω_21,2Q [eV]
E_2J
E_2H
ħω_a
ħω_b
ħω_43 [eV]

Figure 4

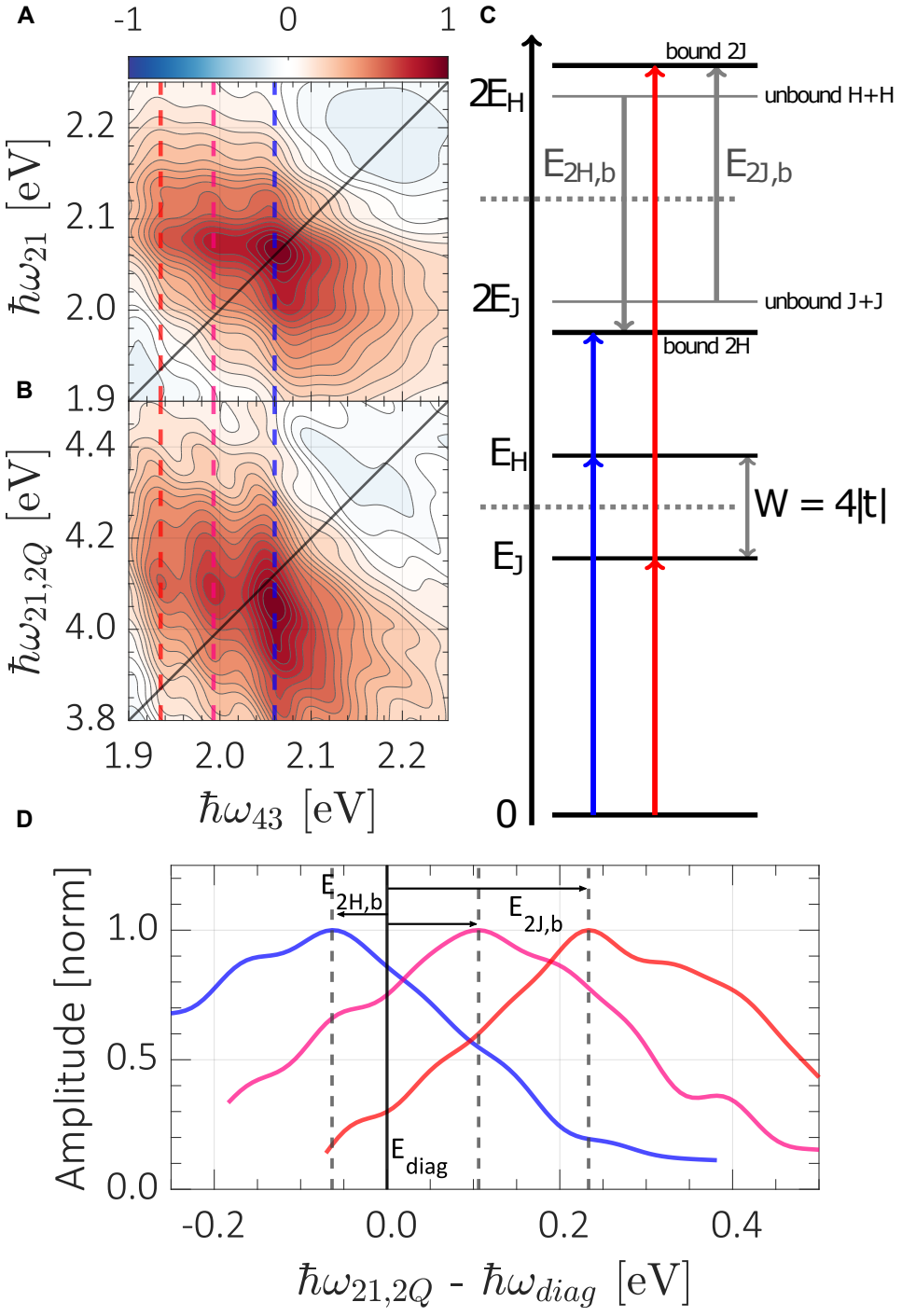
A
B
C
D
-1
0
1
2.2
2.1
2.0
1.9
4.4
4.2
4.0
3.8
$\hbar\omega_{21}$ [eV]
$\hbar\omega_{21,2Q}$ [eV]
1.9
2.0
2.1
2.2
$\hbar\omega_{43}$ [eV]
bound 2J
unbound H+H
$2E_H$
$E_{2H,b}$
$E_{2J,b}$
$2E_J$
unbound J+J
bound 2H
E_H
W = 4|t|
E_J
0
Amplitude [norm]
1.0
0.5
0.0
$E_{2H,b}$
$E_{2J,b}$
E_{diag}
-0.2
0.0
0.2
0.4
$\hbar\omega_{21,2Q}$ - $\hbar\omega_{diag}$ [eV]

Supplementary Materials: The molecular origin of Frenkel biexciton binding

Elizabeth Gutiérrez Meza,[1], Ravyn Malatesta,[1] Hongmo Li,[2]
Ilaria Bargigia,[3] Ajay Ram Srimath Kandada,[3],
David A. Valverde-Chávez,[1] Natalie Stingelin,[2,4]
Sergei Tretiak,[5,6,7] Eric R. Bittner,[8†] and Carlos Silva[1,2,9*]

[1]School of Chemistry and Biochemistry, Georgia Institute of Technology,
901 Atlantic Drive, Atlanta, GA 30332, United States
[2]School of Materials Science and Engineering, Georgia Institute of Technology,
North Avenue, Atlanta, GA 30332, United States
[3]Department of Physics and Center for Functional Materials, Wake Forest University,
1834 Wake Forest Road, Winston-Salem, NC 27109, United States
[4] School of Chemical and Biomolecular Engineering,
311 Ferst Drive NW, Atlanta, GA 30332, United States
[5]Theoretical Division, Los Alamos National Laboratory,
Los Alamos, NM 87545, United States
[6]Center for Nonlinear Studies, Los Alamos National Laboratory,
Los Alamos, NM 87545, United States
[7]Center for Integrated Nanotechnologies, Los Alamos National Laboratory,
Los Alamos, NM 87545, United States
[8]Department of Chemistry, University of Houston, Houston, Texas 77204, United States
[9]School of Physics, Georgia Institute of Technology, 837 State Street,
Atlanta, GA 30332, United States

[†]E-mail address: ebittner@central.uh.edu
[*]Corresponding author; E-mail address: carlos.silva@gatech.edu

1 Materials and Methods

1.1 Sample preparation

PBTTT [poly(2,5-bis(3-hexadecylthiophene-2-yl)thieno[3,2-b]thiophene)] was synthesized as previously reported ($M_n = 38\,\mathrm{kg\,mol^{-1}}$, $Đ_M$ = 1.78) (*17*). PBTTT was dissolved in 1,2-dichlorobenzene (o-DCB, Sigma-Aldrich) at 85°C and the solution was stirred for 1 hour. The concentration of the solution was $10\,\mathrm{mg\,mL^{-1}}$. Films were drop cast at 30°C on sapphire substrates (UQG Optics, 10-mm diameter, 1-mm thickness) from as-prepared solution and were subsequently left dry at this temperature.

1.2 2D-PLE Spectroscopy

1.2.1 Experimental Apparatus

The experimental setup shown in Fig. S1 is derived from the phase-modulation and sensitive detection technique previously developed by Marcus and coworkers (*27*). It consists in a four collinear femtosecond pulses which are generated by means of two Mach-Zehnder interferometers (MZI) that are nested into an outer MZI. We use a regenerative amplifier working at a repetition rate of 300 kHz and generating a pulse train centered at 1030 nm and a pulse duration of 220 fs (Light Conversion Pharos Model PH1-20-0200-02-10). This pulse train output pumps a non-collinear optical parametric amplifier (NOPA) to produce 80-nm bandwidth pulses centered around 605 nm (Light Conversion Orpheus-N-3H). An adaptative $4f$ pulse shaper (Bio-Photonics Solutions FemtoJock-P), pre-compresses the pulse to be 12 fs at the sample position by means of multiphoton intrapulse interference phase scan (MIIPS). The output is split by means of a 50% beam splitter, one arm is delayed with respect to the other using an optical delay line (Aerotech ANT130-060-L-25DU-MP) to define and control the inter-pulse delay, and then recombined in a collinear geometry with another identical beam splitter, defining the outer MZI. Each of these arms of this MZI is split into two sub-arms by 50% beam splitters, one

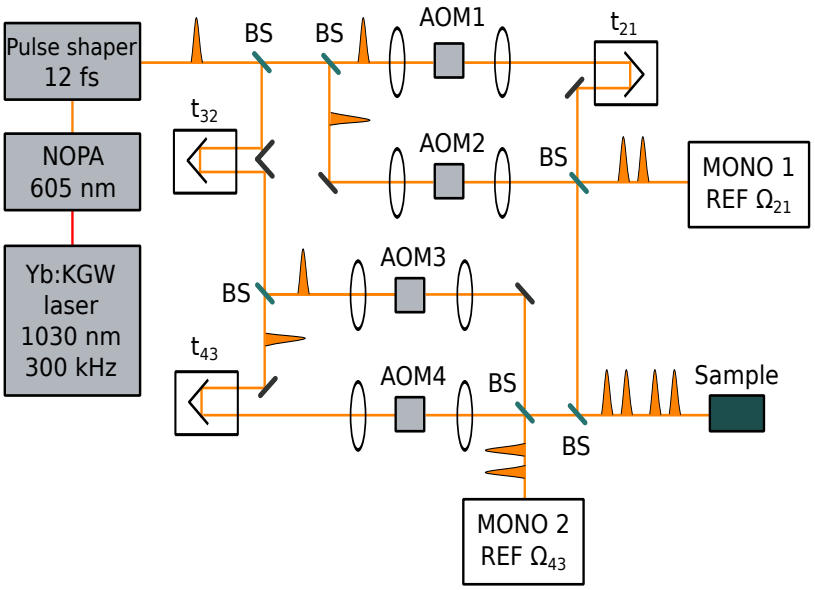

Figure S1: Schematic diagram of the 2D-PLE set up. Yb:KGW: Ytterbium-doped potassium gadolinium tungstate laser. NOPA:Noncollinear optical parametric amplifier. BS:Beam splitter. AOM:Acousto-optic modulator. MONO:Monochromator. REF:Reference signal

of the inner arms in each MZI is delayed with respect to the other with an optical delay line (Aerotech ANT130-035-L-25DU-MP). and recombined to produce a four-pulse sequence. The phase-modulation scheme is achieved by placing an acousto-optic Bragg cell on each arm of the twin MZIs. The Bragg cells produce a frequency shift on each pulse that corresponds to its modulating frequency Ω_i ($i = 1, 2, 3, 4$), at around 200 MHz. The interfering excitation pulses generate a population signal oscillating at $\Omega_{21} = \Omega_2 - \Omega_1$ and $\Omega_{43} = \Omega_4 - \Omega_3$. In this work, we use $\Omega_{21} = 5$ kHz and $\Omega_{43} = 14$ kHz. Within this phase modulation scheme, is possible to isolate the fourth-order contribution to the signal by using a lock-in amplifier (Zurich Instruments UHFLI) with optically generated reference waveforms at $\Omega_{43} \pm \Omega_{21}$. These reference

waveforms are optically constructed by means of avalanche photodiodes (APD) attached to the output of the two monochromators as illustrated in Fig. S1.

For the one-quantum experiment, the linear signals are obtained at the modulation frequencies Ω_{43} and Ω_{21}. The rephasing and non-rephasing contributions to the fourth-order population are extracted by demodulating the signal at sideband frequencies $\Omega_{43} - \Omega_{21}$ and $\Omega_{43} + \Omega_{21}$, respectively. These four signals are acquired simultaneously.

The fourth order population is detected with the temporally integrated photoluminescence (PL) which is collected in a reflection geometry. The PBTTT thin film temperature is maintained at 5 K in a closed-cycle cryostation (Montana Instruments). The PL is isolated from the excitation laser by a long pass filter of 650 nm, the PL signal is then detected by an APD (Hamamatsu C12703-01) and sent to the lock-in amplifier. The 2D maps are acquired by measuring the demodulated PL signal as a function of the time delays t_{21} and t_{43} (coherence times) at a fixed population time t_{32}. In this work the population time was set to $t_{32} = 30$ fs, in order to avoid any artifacts caused by the temporal overlap of the pulse pairs. The raw data obtained in the time-domain are then Fourier-transformed on both t_{21} and t_{43} axes to get 2D maps on the frequency- domain as $\hbar\omega_{21}$ and $\hbar\omega_{43}$, leading to the rephasing and non-rephasing 2D maps.

1.2.2 Second-harmonic demodulation and two-quantum correlations

In order to isolate the two-quantum coherent signals, we based our experiments on the *n*th harmonic lock-in demodulation scheme developed by Bruder et al., in which as single MZI as the inner ones in Fig. S1 was used (*31, 32*). In this work, we demodulate at the second harmonic of the reference frequency Ω_{21} and combine it with the fundamental of Ω_{43}, i.e., we demodulate the integrated PL intensity at the reference frequency $\Omega_{43} + 2\Omega_{21}$. As above, we Fourier-transform the measured two-dimensional coherence function along the variable t_{21} and t_{43} at a fixed value of t_{32}, and obtain a 2D spectrum with energy variables $\hbar\omega_{21,2Q}$ and $\hbar\omega_{43}$,

where $\hbar\omega_{21,2Q}$ corresponds to the two-quantum energy axis. In what follows, we develop the formalism describing how this demodulation scheme results in the two-quantum correlation function of Fig. 4B in the main manuscript, following the initial development in ref. (*27*).

The total electric field $\vec{E}(t)$ is a sum of the four individual pulses $\vec{E}(t) = \vec{E}_1(t) + \vec{E}_2(t) + \vec{E}_3(t) + \vec{E}_4(t)$, where the field of the jth pulse ($j \in \{1, 2, 3, 4\}$) is defined as

$$\vec{E}_j(t) \equiv \vec{A}_j(t - t_j)\cos[\omega_L(t - t_j) + \phi_j], \tag{1}$$

where $\vec{A}_j(t - t_j)$ is the temporal envelope of a pulse arriving at time t_j, ω_L is the laser carrier frequency, and ϕ_j is a constant phase. The Fourier transform yields the frequency-dependent field of pulse j

$$\hat{\vec{E}}_j(\omega) = \hat{\vec{E}}_j^{+}(\omega) + \hat{\vec{E}}_j^{-}(\omega), \tag{2}$$

where $\hat{\vec{E}}_j^{+}$ and $\hat{\vec{E}}_j^{-}$ are the forward and counter-rotating components of the Fourier transform respectively. The components have the explicit forms

$$\hat{\vec{E}}_j^{+}(\omega) = \vec{\alpha}_j(\omega)e^{i\omega t_j - i\phi_j}; \tag{3}$$

$$\hat{\vec{E}}_j^{-}(\omega) = \vec{\alpha}_j(-\omega)e^{i\omega t_j + i\phi_j}, \tag{4}$$

where $\vec{\alpha}_j(\omega)$ and ϕ_j are the spectral amplitude and phase of the jth pulse.

We consider the six pathways to an excited state population shown in Fig. S2 to contribute to the sum and difference frequency signals. In analogy to the Z-terms derived by Tekavec *et al.* (*27*), we derive six Z-terms using a perturbative expansion in the interaction picture. The first-order expansion of the population generated by interaction with pulse j is

$$|\psi_j\rangle = i\sum_{r,s}\left[\int_{-\infty}^{\infty} d\tau e^{i\omega_{rs}\tau}\vec{\mu}_{rs}\cdot\vec{E}_j(\tau)|r\rangle\langle s|g\rangle\right], \tag{5}$$

where the sum is over two possible excited states, the biexciton state or the two-exciton state. Here we include the derivation of the term $Z_2 \propto \langle\psi_{431(1)}|\psi_{2(2)}\rangle$ and then provide the final Z-terms without their explicit derivations.

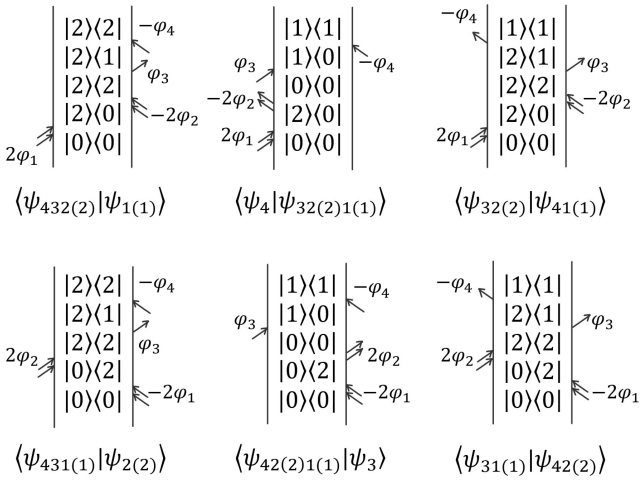

Figure S2: Double-sided Feynman diagrams for the pathways corresponding to (top) the three sum terms and (bottom) three difference terms.

The term Z_2 corresponds to an excited population state in the second excited state generated by a fourth-order population in the bra and a second-order population in the ket. The bra is excited in two cascaded interactions with the first pulse and subsequently de-excited then excited with pulses 3 and 4. The ket is excited in two cascaded interactions with the second pulse. There are four possible pathways matching this interaction order as shown in Fig. S3 where the final population state is either the biexciton (b) or the two-exciton (x) state. The second-order

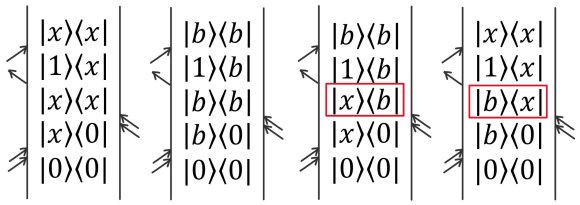

Figure S3: Variations of the pathway of the Z_2 term incorporating the possible biexciton (b) and two-exciton (x) states. The last two diagrams show the dependence of Z_2 on the coupling between these states.

population generated by cascaded interactions with the second pulse is

$$\begin{aligned}
|\psi_{2(2)}\rangle &= i\sum_r \Big[\int_{-\infty}^{\infty} d\tau \vec{\mu}_{r1}\cdot e^{i\omega_{r1}\tau}\vec{E}_2(\tau)\Big]\Big[\int_{-\infty}^{\tau} d\tau' \vec{\mu}_{1g}\cdot e^{i\omega_{1g}\tau'}\vec{E}_2(\tau')\Big]|r\rangle \\
&\cong i\sum_r \Big[\vec{\mu}_{r1}\cdot\hat{\vec{E}}_2^{-}(\omega_{r1})\Big]\Big[\vec{\mu}_{1g}\cdot\hat{\vec{E}}_2^{-}(\omega_{1g})\Big]|r\rangle \\
&= i\sum_r [\vec{\mu}_{r1}\cdot\vec{\alpha}_2(-\omega_{r1})]\,[\vec{\mu}_{1g}\cdot\vec{\alpha}_2(-\omega_{1g})]\,e^{i(\omega_{r1}t_2+\phi_2)}e^{i(\omega_{1g}t_2+\phi_2)}|r\rangle \\
&= i\sum_r [\vec{\mu}_{r1}\cdot\vec{\alpha}_2(-\omega_{r1})]\,[\vec{\mu}_{1g}\cdot\vec{\alpha}_2(-\omega_{1g})]\,e^{i(\omega_{rg}t_2+2\phi_2)}|r\rangle. \qquad (6)
\end{aligned}$$

The fourth-order population generated by cascaded interactions with the first pulse followed by interactions with the third and fourth pulses is

$$\begin{aligned}
|\psi_{431(1)}\rangle = -i\sum_{r,s}\Big[\int_{-\infty}^{\infty} d\tau e^{i\omega_{r1}\tau}\vec{\mu}_{r1}\cdot\vec{E}_4(\tau)\Big]\Big[\int_{-\infty}^{\tau} d\tau' e^{-i\omega_{s1}\tau'}\vec{\mu}_{1s}\cdot\vec{E}_3(\tau')\Big] \\
\times\Big[\int_{-\infty}^{\tau'} d\tau''\vec{\mu}_{s1}\cdot e^{i\omega_{s1}\tau''}\vec{E}_1(\tau'')\Big]\Big[\int_{-\infty}^{\tau''} d\tau'''\vec{\mu}_{1g}\cdot e^{i\omega_{1g}\tau'''}\vec{E}_1(\tau''')\Big]|r\rangle, \qquad (7)
\end{aligned}$$

where we enforce the time-ordering $t_1 < t_2 < t_3 < t_4$. With four independent Fourier transforms and the rotating wave approximation we find

$$\begin{aligned}
|\psi_{431(1)}\rangle &\cong -i\sum_{r,s}\Big[\vec{\mu}_{r1}\cdot\hat{\vec{E}}_4^{-}(\omega_{r1})\Big]\Big[\vec{\mu}_{s1}\cdot\hat{\vec{E}}_3^{+}(-\omega_{s1})\Big]\Big[\vec{\mu}_{s1}\cdot\hat{\vec{E}}_1^{-}(\omega_{s1})\Big]\Big[\vec{\mu}_{1g}\cdot\hat{\vec{E}}_1^{-}(\omega_{1g})\Big]|r\rangle \\
&= -i\sum_{r,s}[\vec{\mu}_{r1}\cdot\vec{\alpha}_4(\omega_{r1})]\,[\vec{\mu}_{s1}\cdot\vec{\alpha}_3(\omega_{s1})]\,[\vec{\mu}_{s1}\cdot\vec{\alpha}_1(\omega_{s1})]\,[\vec{\mu}_{1g}\cdot\vec{\alpha}_1(\omega_{1g})] \\
&\quad\times e^{i(\omega_{r1}t_4+\phi_4)}e^{-i(\omega_{s1}t_3+\phi_3)}e^{i(\omega_{sg}t_1+2\phi_1)}|r\rangle. \qquad (8)
\end{aligned}$$

The inner product $\langle\psi_{431(1)}|\psi_{2(2)}\rangle$ gives

$$\begin{aligned} Z_2 &= \langle\psi_{431(1)}|\psi_{2(2)}\rangle \\ &= e^{-i(\phi_{43}-2\phi_{21})}\Bigg[\sum_e \left[|\vec{\mu}_{e1}|^4|\vec{\mu}_{1g}|^2|\vec{\alpha}(\omega_{e1})|^4|\vec{\alpha}(\omega_{1g})|^2 e^{-i(\omega_{e1}t_{43}-\omega_{eg}t_{21})}\right] \\ &\quad + |\vec{\mu}_{b1}|^2|\vec{\mu}_{x1}|^2|\vec{\mu}_{1g}|^2|\vec{\alpha}(\omega_{b1})|^2|\vec{\alpha}(\omega_{x1})|^2|\vec{\alpha}(\omega_{1g})|^2 \\ &\quad \times \left[e^{-i(\omega_{x1}t_{43}-\omega_{xg}t_{21}+\omega_{xb}t_{32})} + e^{-i(\omega_{b1}t_{43}-\omega_{bg}t_{21}+\omega_{bx}t_{32})}\right]\Bigg], \end{aligned} \tag{9}$$

where the final two terms correspond to coupling pathways in which the system evolves during time t_{32} as $|r\rangle\langle s|$ where $r \neq s$. This is the first of three difference terms in which the phase component is $e^{-i(\phi_{43}-2\phi_{21})}$. In the two-quantum experiment the phase modulation is at the difference frequency $-2\Omega_{21}+\Omega_{43}$ where Ω is used in place of ϕ to highlight the change to the experimental scheme.

Acousto-optic modulation at the sum and difference frequencies ($2\Omega_{21}+\Omega_{43}$ and $-2\Omega_{21}+\Omega_{43}$, respectively) followed by demodulation using a lock-in amplifier allows for the simultaneous measurement of the sum and difference frequency signals for all interpulse delay times. The phase modulation gives $\Omega_{21} = \Phi_{21}t' + \Omega_{21}^{\circ}$ and $\Omega_{43} = \Phi_{43}t' + \Omega_{43}^{\circ}$ where t' is a quasicontinuous time variable and Ω_{21}° and Ω_{43}° are constant phases. The forward-rotating term for the frequency-dependent electric field of pulse j with phase modulation becomes

$$\hat{\vec{E}}^{+}_{m,j}(\omega) = \vec{\alpha}_j(\omega)e^{i\omega(t_j+mT)-i\Phi_j mT}, \tag{10}$$

where m is the number of repetitions of pulse j and T is the time between each repetition. The phase component $\Omega_{m,j} = \Phi_j mT$ incrementally increases by $\Phi_j T$ with each successive repetition. Lock-in demodulation at the sum and difference frequencies are used to isolate the

populations corresponding to each Z-term. The remaining Z-terms are

$$\begin{aligned} Z_1 &= \langle \psi_{432(2)} | \psi_{1(1)} \rangle \\ &= e^{-i(\phi_{43}+2\phi_{21})} \Bigg[\sum_e \left[|\vec{\mu}_{e1}|^4 |\vec{\mu}_{1g}|^2 |\vec{\alpha}(\omega_{e1})|^4 |\vec{\alpha}(\omega_{1g})|^2 e^{-i(\omega_{e1}t_{43}+\omega_{eg}t_{21})} \right] \\ &\quad + |\vec{\mu}_{b1}|^2 |\vec{\mu}_{x1}|^2 |\vec{\mu}_{1g}|^2 |\vec{\alpha}(\omega_{b1})|^2 |\vec{\alpha}(\omega_{x1})|^2 |\vec{\alpha}(\omega_{1g})|^2 \\ &\quad \times \left[e^{-i(\omega_{x1}t_{43}+\omega_{xg}t_{21}+\omega_{xb}t_{32})} + e^{-i(\omega_{b1}t_{43}+\omega_{bg}t_{21}+\omega_{bx}t_{32})} \right] \Bigg], \end{aligned} \tag{11}$$

$$Z_3 = \langle \psi_{42(2)1(1)} | \psi_3 \rangle = e^{-i(\phi_{43}-2\phi_{21})} \left[\sum_e \left[|\vec{\mu}_{1g}|^4 |\vec{\mu}_{e1}|^2 |\vec{\alpha}(\omega_{1g})|^4 |\vec{\alpha}(\omega_{e1})|^2 e^{-i(\omega_{1g}t_{43}-\omega_{eg}t_{21})} \right] \right], \tag{12}$$

$$Z_4 = \langle \psi_4 | \psi_{32(2)1(1)} \rangle = e^{-i(\phi_{43}+2\phi_{21})} \left[\sum_e \left[|\vec{\mu}_{1g}|^4 |\vec{\mu}_{e1}|^2 |\vec{\alpha}(\omega_{1g})|^4 |\vec{\alpha}(\omega_{e1})|^2 e^{-i(\omega_{1g}t_{43}+\omega_{eg}t_{21})} \right] \right], \tag{13}$$

$$Z_5 = \langle \psi_{32(2)} | \psi_{41(1)} \rangle = Z_1, \tag{14}$$

and

$$Z_6 = \langle \psi_{31(1)} | \psi_{42(2)} \rangle = Z_2, \tag{15}$$

where Z_5 and Z_6 correspond to interactions of third-order populations.

It is important to note that for this two quantum experiment, the sums are indexed over two-quantum excited states, $|b\rangle$ and $|x\rangle$, such the $\omega_{eg} \sim 2\Omega$, the second harmonic. For this experiment, the excitations and deexcitations at times t_3 and t_4 are still one-quantum transitions $\sim \Omega$.

The total sixth-order population can be divided between sum and difference terms

$$n^{(6)}(t_{43}, t_{32}, t_{21}) = n^{(6)}_{sum}(t_{43}, t_{32}, t_{21}) + n^{(6)}_{dif}(t_{43}, t_{32}, t_{21}), \tag{16}$$

where

$$n^{(6)}_{sum}(t_{43}, t_{32}, t_{21}) = \frac{2}{\hbar^6}\Re(2Z_1 + Z_4) \tag{17}$$

and

$$n^{(6)}_{dif}(t_{43}, t_{32}, t_{21}) = \frac{2}{\hbar^6}\Re(2Z_2 + Z_3). \tag{18}$$

Mukamel has criticized the scheme of Bruder et al. as being unselective for multi-quantum responses of non-interacting particles (*33*). He argued that for a particle ensemble, the photoluminescence signal reported in ref. 31 is given by a simple product of one-particle coherences:

$$P^{(2)}(\tau) = N(N-1)|\mu_{eg}|^4 E_1^2 E_2^2 \exp(-2i(\omega_{eg} - \omega_1)\tau - 2i\phi_{21}), \tag{19}$$

with τ being the interpulse delay, and μ_{eg} the $|g\rangle \rightarrow |e\rangle$ transition dipole matrix element. By measuring the $2\phi_{21}$ phase component, he argued that one observes $|e_j e_k\rangle$ and not $|e_j g_k\rangle$ coherences, which would correspond to the two-particle resonance. Nevertheless, the expression in eq. 19 *only* considers the contribution form incoherent population mixing, which we rule out below in Section 1.2.3. Given the way that the desired signal is filtered by the high-pass filter of the lockin amplifier, the only possible contribution is therefore from the coherent Louiville pathways outlined above.

1.2.3 Incoherent population mixing contributions

In condensed matter systems, photoexcitations are mobile and prone to inter-particle interactions such as exciton bimolecular annihilation, scattering processes and Auger recombination. These processes result in a nonlinear population dynamics that arises from linear light-matter interactions and contributes as an incoherent signal to the measured lineshape (*34, 35*), masking the true 2D coherent response. According to Karki et al, these contributions can be differentiated from the true nonlinear signal by analyzing the phase and amplitude of the linear signal,

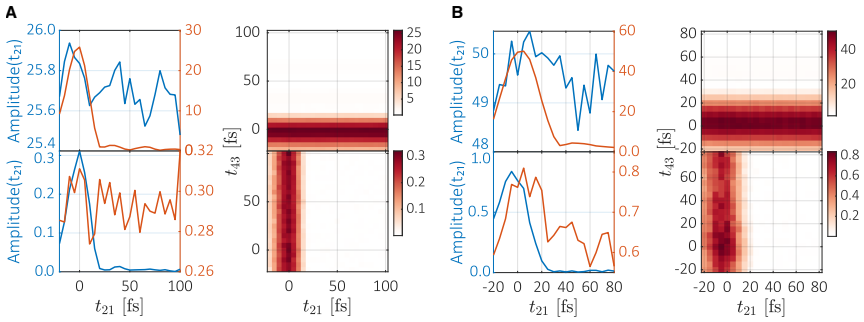

Figure S4: **Amplitude maps of the linear 2Q signal**
Measured with fluences of (**A**) $63\,\mathrm{nJ\,cm^{-2}}$ and (**B**) $251\,\mathrm{nJ\,cm^{-2}}$, respectively. Cuts of the amplitude maps along the t_{21} direction (right axis in red) and the t_{43} direction (left axis in blue).

they show that the mixed signal have a π phase shift with respect to the true nonlinear signal. As pointed out in that work, the phase shift can be precisely identified if the linear and nonlinear signals are acquired simultaneously over the lock-in detection. This being the case of the measurements presented here, we performed this analysis and show the amplitude maps of the linear signals. The time-domain linear response of the two-quantum correlation spectra corresponding to the $(\Omega_{43} + 2\Omega_{21})$ signal, is presented in Fig. S4. This response was measured at $63\,\mathrm{nJ\,cm^{-2}}$ panel (**A**) and $251\,\mathrm{nJ\,cm^{-2}}$, (**B**) respectively. Both panels show the amplitude spectrum obtained by scanning along t_{21} for the each value along t_{43}, and also the cuts of this amplitude map along both temporal axis, at frequencies Ω_{43} (top) and $2\Omega_{21}$ (bottom). In panel (**A**), when scanning along t_{21}, it is expected a constant signal as shown in the cut along this temporal axis, while a cut along t_{43} shows a maximum amplitude intensity. For a high fluence regime as displayed on panel (**B**), the incoherent mixing contribution to the signal is manifested by the presence of a crosstalk which can be observed in the amplitude map at the bottom.

The comparison of the 2DPLE spectra of the real part of the $(\Omega_{43} + 2\Omega_{21})$ signal at low and

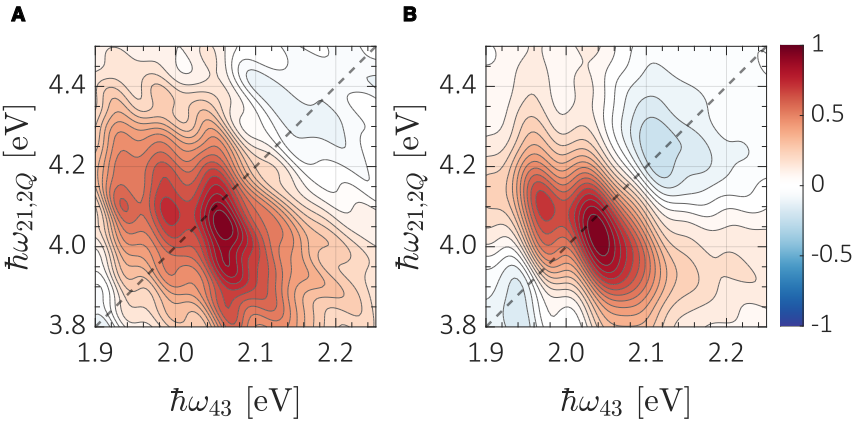

Figure S5: **Comparison of the real part of the 2Q signal at different fluences** Real part of the non-rephasing signal ($f_{\mathrm{ref}} = \Omega_{43} + 2\Omega_{21}$)(**A**) $63\,\mathrm{nJ\,cm^{-2}}$ and (**B**) $251\,\mathrm{nJ\,cm^{-2}}$, respectively.

high fluences, is shown in Fig. S5. For a low fluence regime as shown in panel (**A**), we observe a well defined features that correspond to the two quantum attractive and repulsive interactions as discussed in the main text. On the other side, panel(**B**) shows the spectra acquired by using high fluence, it is evident that there are less structured features specially along the two-quantum energy axis $\hbar_{21,2Q}$. The pump spectra has a bit less bandwidth for the spectrum shown on panel(**B**), missing the lowest energy feature at 1.94 eV , however it is clear the incoherent mixing effect on the 2D maps.

1.3 Density Functional Theory Calculations

All DFT calculations were carried out with the Gaussian 16, Revision A.03 software package, (*36*) using the B3LYP hybrid functional and the 6–31G* basis set. The PBTTT chain was cut down into a trimer unit, and the hexadecyl side chains were replaced by ethyl groups in

order to reduce the computational cost. The structure of oligomers were first optimized, and the ground state dipole moment was obtained from single point calculations. Excited states were calculated on top of the geometrical optimized structure using TD-DFT, and the excited state dipole moment and transition dipole moment were retrieved from the results corresponding to the first excited state before relaxation. The results are visualized using Avogadro. (*37*)

2 2D-PLE Supplementary Results

2.1 2D-PLE One- and Two-Quantum Spectra

Fig. S6 shows the real and imaginary parts of the rephasing(**A, B**) one-quantum, non-rephasing (**C,D**), and two-quantum coherence (**C,D**) phase combination of the 2D-PLE spectra at 5 K and population waiting time $t_{32} = 30\,\mathrm{fs}$

2.2 Spectral Analysis of Two-Quantum Spectrum

E (eV)	$E_{\mathrm{2J,b}}$ (meV)	$E_{\mathrm{2H,b}}$ (meV)
2.06	-170 ± 6	138 ± 8
	-64 ± 6	258 ± 8
1.99	-149 ± 6	106 ± 6
	-57 ± 6	198 ± 6
		276 ± 6
		389 ± 6
1.94	-35 ± 6	53 ± 8
		233 ± 6
		329 ± 8
		421 ± 8

Table 1: **Attractive and repulsive interaction energies** corresponding to Fig. 4 in the main text.

3 Supplementary Theoretical Modeling

3.1 Biexciton bound-states

Two excitons become bound when their mutual attraction is sufficient to overcome their kinetic energy. To examine this in the framework of the tight-binding model developed in manuscript, we take a continuum limit and work in a relative coordinate reference frame where $x = |r_1 - r_2|$ is the separation between two localized excitons. Thus, the Schrödinger equation can be approximated as

$$t\psi'' + U\delta(x)\psi = E\psi. \tag{20}$$

For bound states, $\psi(x)$ must vanish as $x \to \pm\infty$, giving that

$$\psi(x) = \begin{cases} \sqrt{\kappa}e^{-\kappa x} & x > 0 \\ \sqrt{\kappa}e^{+\kappa x} & x < 0 \end{cases} \tag{21}$$

where $\kappa = U/2t$ is a positive constant and $E = t\kappa^2$. In general, we take $t = -\hbar^2/2\mu_{eff}$ and $U < 0$ for an attractive potential giving rise to a bound state energetically *below* the continuum for the scattering states.

For molecular aggregates, the transfer integral t depends upon the relative orientation of the transition moments between the exciton donor and acceptor sites and varies as $t = |\mu_{ge}|^2(1 - 3\cos^2(\theta))/R^3$ where θ is the relative orientation of the two transition moments and R is the separation between the two species (taking z to be along the direction connecting the two molecular centers). For J-aggregates, $\theta \approx 0$ for "head-to-tail" coaxial alignment of transition dipoles giving $t < 0$ and $\mu_{eff} > 0$ while for H-aggregates $\theta \approx \pi/2$ corresponding to the dipoles being aligned perpendicular to z in which $t > 0$ and hence $\mu_{eff} < 0$. Optically, the bright state for a J-aggregate lies at the bottom of the energy band while the bright state for an H-aggregate lies at the top. This implies that two kinds of bound biexciton species could exist in systems such as PBTTT which is well-known for having both H and J-like character.

Fig. S7 shows the radial correlation function $g(r)$ between excitons and the total biexciton energy for various parametric choices of the tight-binding model discussed in the main paper. We define this such that value $g(0)$ is the probability of finding the two excitons on two directly adjacent sites since Pauli exclusion prevents two excitons for occupying the same site. For the homogeneous system ($\Delta = 0$), we see that biexcitons are stable only for $|U/t| > 2$. Below this, each exciton is delocalized over 1/2 the system.

For the homogeneous system, $\Delta = 0$, the exciton-exciton radial distribution falls off exponentially with increasing exciton/exciton separation, consistent with the continuum model given above. Recall that Δ is a measure of the energy difference between adjacent tight-binding sites and that increasing Δ introduces an energy cost for having two adjacent excitons, which we referred to as the crenelation. As Δ increases, the biexciton becomes unstable and dissociates into a pair of free excitons. Since our model calculations use a finite number of tight-binding sites (in this case 100) with periodic boundary conditions, the two "free" excitons are maximally separated to opposite sides of the periodic "ring". The oscillation in $g(r)$ reflects the fact that the odd-numbered sites have lower energy than the even-numbered sites and as such a single exciton is more likely to be in an odd-numbered sites.

Finally, we note that the exciton model we present is applicable to both H and J-like coupling schemes. In the manuscript, we show results for $t < 0$ and $U < 0$, which are somewhat more intuitive to understand. When used for the $t > 0$ and $U > 0$ case, the bound biexciton will lie at the top of the energy spectrum above the continuum of scattering states rather than below the free-exciton continuum.

References

31. L. Bruder, M. Binz, F. Stienkemeier, *Phys. Rev. A* **92**, 053412 (2015).

32. L. Bruder, U. Bangert, F. Stienkemeier, *Opt. Express* **25**, 5302 (2017).

33. S. Mukamel, *J. Chem. Phys.* **145**, 041102 (2016).

34. P. Grégoire, *et al.*, *J. Chem. Phys.* **147**, 114201 (2017).

35. A. A. S. Kalaee, F. Damtie, K. J. Karki, *J. Phys. Chem. A* **123**, 4119 (2019).

36. M. J. Frisch, *et al.*, Gaussian 16 Revision A.03 (2016). Gaussian Inc. Wallingford CT.

37. M. D. Hanwell, *et al.*, *Journal of cheminformatics* **4**, 17 (2012).

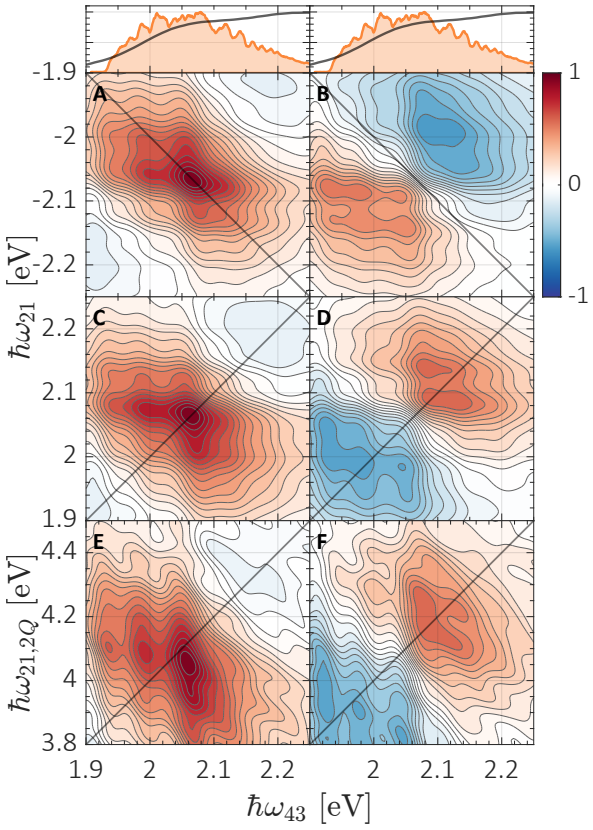

Figure S6: **One and two quantum 2D-PLE spectra measured at 5 K and $t_{32} = 30$ fs.** The laser spectrum (filled orange line) and the linear absorption spectrum (black line) are shown on the top panel for reference. Black line along the diagonal (**A, B**) The real and imaginary part of the one-quantum rephasing ($f_{\mathrm{ref}} = \Omega_{43} - \Omega_{21}$) spectra. (**C, D**) The real and imaginary part of the one-quantum non-rephasing ($f_{\mathrm{ref}} = \Omega_{43} + \Omega_{21}$) spectra. (**E, F**) The real and imaginary part of the two-quantum ($f_{\mathrm{ref}} = \Omega_{43} + 2\Omega_{21}$)) spectra.

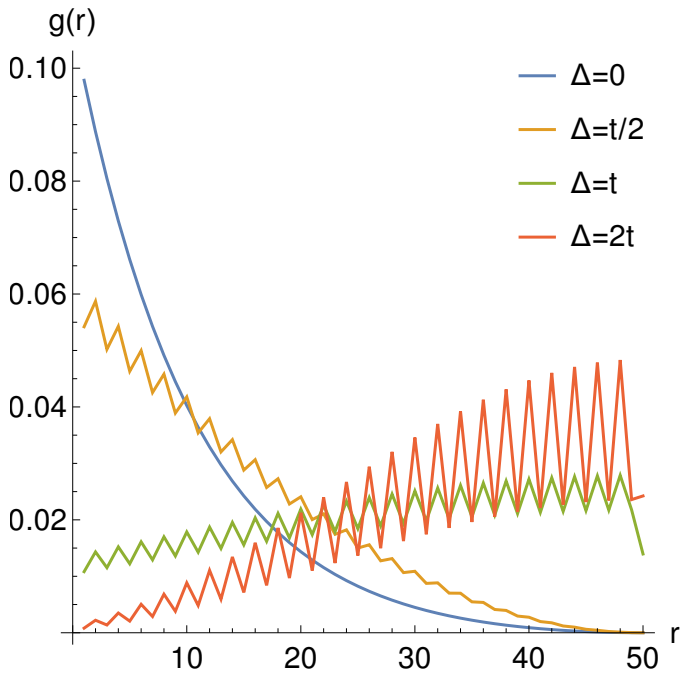

Figure S7: Bi-exciton pair distribution function for bound and un-bound pairs.